# $NO_2$ Quantum Yield from the 248 nm Photodissociation of Peroxynitric Acid ($HO_2NO_2$)†

**Coleen M. Roehl,‡ Troy L. Mazely,§ Randall R. Friedl, Yumin Li,⊥ Joseph S. Francisco,⊥ and Stanley P. Sander***

*Jet Propulsion Laboratory, California Institute of Technology, 4800 Oak Grove Drive, Pasadena, California 91109*

*Received: May 31, 2000; In Final Form: October 31, 2000*

Peroxynitric acid (PNA) was photolyzed at 248 nm, and the $NO_2$ photoproduct was detected by laser-induced fluorescence (LIF). The quantum yield for the production of $NO_2$ was determined by comparison with $HNO_3$ photolysis data taken under identical experimental conditions. Measurements made over a range of pressures, flows, and precursor concentrations resulted in an $NO_2$ quantum yield of $0.56 \pm 0.17$, where the statistical uncertainty is 2 standard deviations. Calculations of potential energy curves for several low-lying singlet and triplet states of PNA are presented. The calculations show that while the singlet excitations occur via an $n-\pi^*$ transition on the $NO_2$ moiety, the dissociative channels forming $OH + NO_3$ and $HO_2 + NO_2$ likely occur via predissocation on different surfaces. Excitation energies at the MRCI and CCSD(T) level of theory show that excited states of PNA are not accessible at wavelengths longer than 407 nm (~3.0 eV).

## Introduction

Investigations of the atmospheric impacts of aircraft emissions,[1,2] industrial and agricultural emissions,[3] and changes in the radiative balance of the atmosphere[4] invariably focus on the chemical mechanisms which control the production and loss of ozone. These mechanisms are strongly influenced by species which couple the members of different chemical families. An example is peroxynitric acid, $HO_2NO_2$, which couples odd hydrogen ($HO_x$) and odd nitrogen ($NO_x$) in the upper troposphere and lower stratosphere. PNA is formed by the recombination reaction

$$HO_2 + NO_2 + M \rightarrow HO_2NO_2 + M$$

and removed mainly by reaction with OH, photolysis, and thermal decomposition. PNA plays a key role in the destruction of $HO_x$ radicals by the catalytic cycle

$$HO_2 + NO_2 + M \rightarrow HO_2NO_2 + M$$

$$OH + HO_2NO_2 \rightarrow NO_2 + H_2O + O_2$$

Net: $$OH + HO_2 \rightarrow H_2O + O_2$$

PNA also acts as a temporary reservoir for $HO_x$ and $NO_x$ radicals.

Atmospheric models currently consider two PNA photodissociation pathways (thresholds are derived from tabulated thermodynamic data[5]):

$$HO_2NO_2 + h\nu \rightarrow HO_2 + NO_2 \quad \lambda_T = 1230 \pm 120 \text{ nm} \quad (1a)$$

$$\rightarrow OH + NO_3 \quad \lambda_T = 725 \pm 60 \text{ nm} \quad (1b)$$

where the threshold wavelengths are derived from thermodynamic data at 298 K.[5] The atmospheric modeling community uses values of 0.67 and 0.33 for the quantum yields for channels 1a and 1b, respectively, over the entire ultraviolet spectrum of PNA. Other photodissociation channels and their thresholds are

$$HO_2NO_2 + h\nu \rightarrow O(^3P) + HNO_3 \quad \lambda_T = 718 \text{ nm} \quad (1c)$$

$$\rightarrow H + NO_2 + O_2 \quad \lambda_T = 394 \text{ nm} \quad (1d)$$

$$\rightarrow OH + NO_2 + O(^3P) \quad \lambda_T = 320 \text{ nm} \quad (1e)$$

$$\rightarrow HO_2 + NO + O(^3P) \quad \lambda_T = 296 \text{ nm} \quad (1f)$$

Although there have been a number of measurements of PNA cross sections in the 200−350 nm spectral region,[6−10] relatively little work has been carried out on photodissociation quantum yields. The only study is that of MacLeod et al., who measured the quantum yield for OH formation from PNA photolysis at 248 nm.[11] In the latter study, the OH product yield from PNA photolysis was measured relative to that from $H_2O_2$ in a very low pressure photolysis reactor/mass spectrometer system. A quantum yield of $34 \pm 16\%$ was determined for the production of OH radicals, implying a quantum yield of roughly 66% for the $NO_2 + HO_2$ product channel. Difficulty in measuring absolute, unambiguous PNA concentrations by mass spectrometry complicated their results.

The weak $HO_2-NO_2$ bond in PNA results in a photodissociation threshold which lies in the near-infrared and can be broken by a process mediated by overtones and combination bands involving the O−H stretching mode.[12] This mechanism has been invoked to explain the observed dependence of OH and $HO_2$ at high solar zenith angles in the lower stratosphere.[13] While cross sections of the second and third overtone bands

† Part of the special issue "Harold Johnston Festschrift".

* Also with the Division of Geological and Planetary Sciences, and Division of Engineering and Applied Science, California Institute of Technology, Pasadena, CA 91125. To whom correspondence should be addressed. E-mail: ssander@jpl.nasa.gov. FAX: (818) 393-5019. Address: M/S 183-901, Jet Propulsion Laboratory, 4800 Oak Grove Dr., Pasadena, CA 91109.

‡ Present address: Division of Geological and Planetary Sciences, California Institute of Technology, Pasadena, CA 91125.

§ Present address: Science Applications International Corporation, 21151 Western Ave, Torrance, CA 90501.

⊥ Department of Chemistry and Department of Earth and Atmospheric Sciences, Purdue University, West Lafayette, IN 47907-1393.

10.1021/jp001982x CCC: $20.00 
Published on Web 12/22/2000

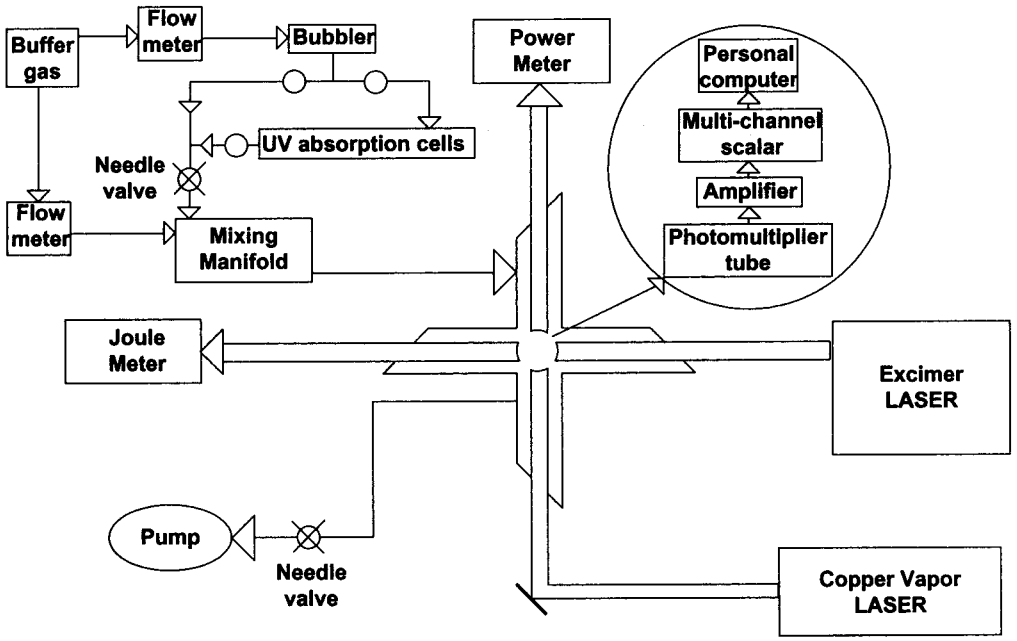


**Figure 1.** Diagram of the experimental apparatus. Details of the optical configuration of the detection axis are presented in the text.

($3\nu_1$ and $4\nu_1$) have been measured recently in solution[14] and gas phase,[15] there are as yet no photodissociation quantum yield measurements for these or other infrared bands.

In this study, PNA was photolyzed at 248 nm and $NO_2$ photoproduct was detected by laser-induced fluorescence (LIF). PNA vapor concentrations were calculated from on-line ultraviolet (UV) absorption measurements. The $NO_2$ quantum yield from PNA was determined by comparison to $HNO_3$ photolysis data taken under identical experimental conditions. The quantum yield was investigated as a function of total flow rate and total pressure over a range of precursor concentrations. Similar photolysis experiments with $HNO_3$ and PAN (peroxyacetyl nitrate) have been performed in this lab.[16−18] The experimental results are complemented by calculations of the ground and excited state potential surfaces which help to rationalize the measured quantum yield.

## Experimental Section

The apparatus used in this study has been thoroughly described in previous publications;[16−18] hence only a brief description along with the slight modifications and particular experimental conditions will be discussed here. A diagram of the apparatus is shown in Figure 1. Gaseous PNA or $HNO_3$ was introduced into a flowing system by passing a calibrated Ar flow through either a PNA or $HNO_3$ sample, which was contained in a quartz reservoir placed in an ice bath. Ar was chosen as the carrier gas because of its relatively slow diffusivity and low fluorescence quenching efficiency. The pressure in the reservoirs (30−100 Torr) was adjusted using a Teflon needle valve located between the reservoirs and a quartz photolysis cell and was monitored with a 100 Torr MKS Baratron capacitance manometer. Typical Ar flows through the reservoirs were 30−100 standard $cm^3\ min^{-1}$ (sccm). Also located upstream of the needle value were two bypass cells (5 and 30 ± 0.1 cm in length)used during UV absorption measurements. The precursor gases were further diluted with Ar in a mixing volume downstream of the needle valve and before entering the photolysis cell. The partial pressure of the precursors was maintained low enough so that the fluorescence quenching was dominated by the Ar carrier gas. The residence time in the photolysis cell was adjusted by varying the total flow rates between 500 and 1400 sccm and the photolysis cell pressure, which was maintained at 3.0, 7.0, or 10.0 Torr. These conditions ensured that the $NO_2$ photoproduct was removed from the detector viewing zone between excimer pulses.

An excimer laser operated at 248 nm with an energy density of 75 $mJ/cm^2$ and at a repetition rate of 30 Hz was used to photolyze the PNA and $HNO_3$ precursors. The weakly focused excimer beam entered and exited the photolysis cell through quartz windows located perpendicular to flow of gas and attached to the body of the photolysis cell by O-ring joints. By separating the windows from the cell body with O-ring joints and adding blackened baffles in the extended sidearms of the photolysis cell, the fluorescence background induced by the excimer laser was reduced. A portion of pure carrier gas flow was directed through the sidearms to keep the dead volume flushed during measurements. Typically 16 000 laser shots were averaged for one experiment (approximately 10 min).

The 511 nm line of a 10 kHz pulsed copper vapor (probe) laser with ∼2 W of power was utilized for LIF detection of $NO_2$. Light emitted from the copper vapor laser was passed through two dichroic filters, to eliminate the 578 nm line of the copper vapor laser, and telescoping optics, to reduce the beam diameter to about 0.5 cm, before entering the photolysis cell. The high repetition frequency of the probe laser allowed for the acquisition of LIF data points every 100 $\mu$s.

Fluorescence from the excited $NO_2$ was detected by a cooled photomultiplier tube (PMT; Burle C31034-02) that was oriented perpendicular to the laser beam axes. Collection optics served to focus the light onto the cathode of the PMT. Blackened baffles lining the housing tube leading to the PMT and a quartz window (rather than Pyrex) were utilized to reduce undesirable background fluorescence from the excimer laser and scattered light. A 3.8 cm long quartz cell, filled with 0.36 M $K_2Cr_2O_7$ and containing an aluminum honeycomb baffle, were used to filter out scattered light below about 530 nm. Finally, a 578 nm notch filter selectively eliminated any residual Cu vapor emission at that wavelength. The LIF signal was amplified, discriminated, and counted with a multichannel scalar card configured with 10 $\mu$s bin widths, and stored on a PC.

Nitric acid was prepared by collecting the vacuum distillate of a 50:50 by volume mixture of 95% $H_2SO_4$ with $NaNO_3$. The $HNO_3$ was maintained at 0 °C by placing the sample in an ice bath. Peroxynitric acid was synthesized by the reaction of $H_2O_2$ (>90%) with $NO_2BF_4$ using the procedure described by Kenley et al.[19] 90% $H_2O_2$ was prepared by a vacuum distillation of 70% Semiconductor Grade $H_2O_2$ (FMC Corporation), and gravimetric techniques were used to verify the percent composition.

The PNA synthesis method of Kenley et al. produces several impurities that must be removed and/or quantified by careful analysis before use in photodissociation experiments. The spectra of a number of different PNA samples were obtained off-line from the photodissociation experiment using mid-infrared Fourier transform infrared (FTIR) and near-infrared long-path absorption/diode array spectrometer techniques. PNA fundamental vibrational bands ($\upsilon_2-\upsilon_7$) as well as bands from $HNO_3$, $SiF_4$, $H_2O_2$, $H_2O$, and $NO_2$ impurities were identified in the mid-IR spectra, and $HNO_3$, $H_2O_2$, $H_2O$ overtone bands, and $NO_2$ electronic bands were identified in the near-IR spectra.[15] Compositions of the samples were determined using literature values of cross sections and band strengths for both spectral regions.[15,20,21] The dependence of the impurity levels as a function of the PNA sample age has been discussed by Li et al.[22] and Zhang et al.,[15] who found that both $NO_2$ and $HNO_3$ decreased with time due to fractional distillation. In the present work it was found that the ratio [PNA]/[$HNO_3$] was ~10−33 while the ratio [PNA]/[$H_2O_2$] ranged from ~0.5 to 5. The $NO_2$ band centered near 1600 $cm^{-1}$ was observed in spectra of freshly made samples, but decreased rapidly after several minutes of bubbling. No attempt was made to quantify this impurity. The $SiF_4$ and $H_2O$ impurities were not quantified since they do not absorb in the 210−250 nm spectral region and hence could not interfere with the on-line UV absorption measurements (discussed below), nor do they interfere with the quantum yield determinations.

Concentrations of PNA and $HNO_3$ in the photolysis cell were determined immediately before and/or after every photolysis experiment by passing the gas flows through parallel 5 and 30 cm long UV absorption cells upstream of the photolysis cell. UV absorption measurements were made at two wavelengths, 214 nm (Zn lamp, 5 cm cell) and 254 nm (Hg Pen Ray lamp, 30 cm cell), and then were used along with calibrated flow rates and the Beer−Lambert law to calculate vapor concentrations in the photolysis cell. Vapor concentrations obtained at the two wavelengths were compared and averaged. In the $HNO_3$ photolysis experiments, vapor pressures inferred from the photometric measurements were always within several percent of each other and typically in the range of 13.5−14.5 Torr, in excellent agreement with known vapor pressures for pure $HNO_3$ at 0 °C.[23] In the PNA photolysis experiments, the photometric measurements provided a way to measure the fractional impurity of $HNO_3$. This is possible because there is a significant difference in the ratio $\sigma^{\lambda}_{PNA}/\sigma^{\lambda}_{HNO_3}$ at $\lambda = 254$ and 214 nm (the values are 18 and 4.1, respectively). It was found that the vapor pressure of the PNA samples varied over the range 0.3−1.0 Torr depending on the age of the sample. Differences in the PNA concentrations obtained at the two wavelengths were usually less than 10%, and samples with concentrations differing by more than 20% (implying a significant $HNO_3$ impurity) were discarded. Unlike $HNO_3$, the $H_2O_2$ impurity in the PNA sample could not be checked in the on-line UV absorption cells because the ratio $\sigma^{\lambda}_{PNA}/\sigma^{\lambda}_{H_2O_2}$ does not differ significantly between 254 and 214 nm (5.4 and 5.8, respectively). The infrared spectra provided a means for estimating the $H_2O_2$ impurity as a function of sample age, and new PNA samples were produced when the measured PNA vapor pressure dropped by 50%. Since $H_2O_2$ photolysis at 248 nm has no effect on the $NO_2$ signal, the primary effect of $H_2O_2$ impurity is to introduce a small error in the determination of [PNA].

After further dilution, the concentration ranges of photolyte in the PNA and $HNO_3$ photolysis experiments were $(1-43) \times 10^{13}$ $cm^3$ and $(2-23) \times 10^{14}$ $cm^3$, respectively.

## Computational Methods

The ground state of $HO_2NO_2$ was optimized at the CCSD(T) level of theory[24] with the cc-pVDZ basis set.[25] At the optimized geometry of the ground state, the vertical excitation energies for the lowest two singlet excited states, $2^1A$ and $3^1A$, and the lowest two triplet excited states, $1^3A$ and $2^3A$, are calculated at the complete active space self-consistent field (CASSCF)[26,27] and multireference internally contracted configuration interaction (MRCI)[28,29] level of theory with the cc-pVDZ basis set. The potential energy curves for the $1^1A$, $2^1A$, and $3^1A$ states are calcualated at the CASSCF level of theory with the cc-pVDZ basis set along the $R_{O-O''}$, $R_{O''-N}$, and $R_{N-O'}$ coordinates, separately, while fixing other parameters at their equilibrium values of the ground state (see Figure 4 for coordinate nomenclature). Some calculations were also carried out for the potentials along the $R_{O-O''}$ coordinate using the aug-cc-pVDZ basis set which inclues diffuse functions. Inclusion of the diffuse functions did not change the resulting potential surfaces significantly.

The active space used for the CASSCF calculation in this work is (16e,11mo), which includes eight doubly occupied molecular orbitals and three virtual molecular orbitals. The size of the CAS in this active space is 9075 CSFs (configuration state functions) for the singlet states and 13 068 CSFs for the triplet states.

## Results

Temporal fluorescence data following the photolysis of PNA and $HNO_3$ were collected over a range of concentrations, pressures, and flow rates in 10 $\mu$s bins. Background noise from cell and filter fluorescence induced by the excimer laser, which decays more rapidly than the LIF signal, was easily deduced from data collected between probe pulses and was subtracted from these raw data. The residual LIF signal consisted of (1) $NO_2$ generated from PNA or $HNO_3$ photolysis, (2) $NO_2$ from PNA or $HNO_3$ decomposition, and (3) probe laser scatter through the optical and chemical filters. These temporal profiles were collected until the $NO_2$ photoproduct completely left the detection viewing zone, at which time the LIF signal was constant and solely resulted from processes 2 and 3 above. The fluorescence signal from the PNA photofragment was calculated by subtracting this constant background signal. Typical curves generated from the photolysis of PNA for 3.0, 7.0, and 10.0 Torr total pressure are illustrated in parts a, b, and c, respectively, of Figure 2. Similar plots were obtained for $HNO_3$ photolysis in experiments performed immediately before or after the PNA measurements.

The temporal fluorescence signals such as those shown in Figure 2 are proportional to the $NO_2$ concentrations present at a particular time after the photolysis pulse and can be related to the $NO_2$ quantum yield (from PNA or $HNO_3$ photolysis) by the following equation:

$$[NO_2]_i = \Lambda \phi_i^{NO_2}(\lambda_{photo})[i]\sigma_i(\lambda_{photo}) \qquad (2)$$

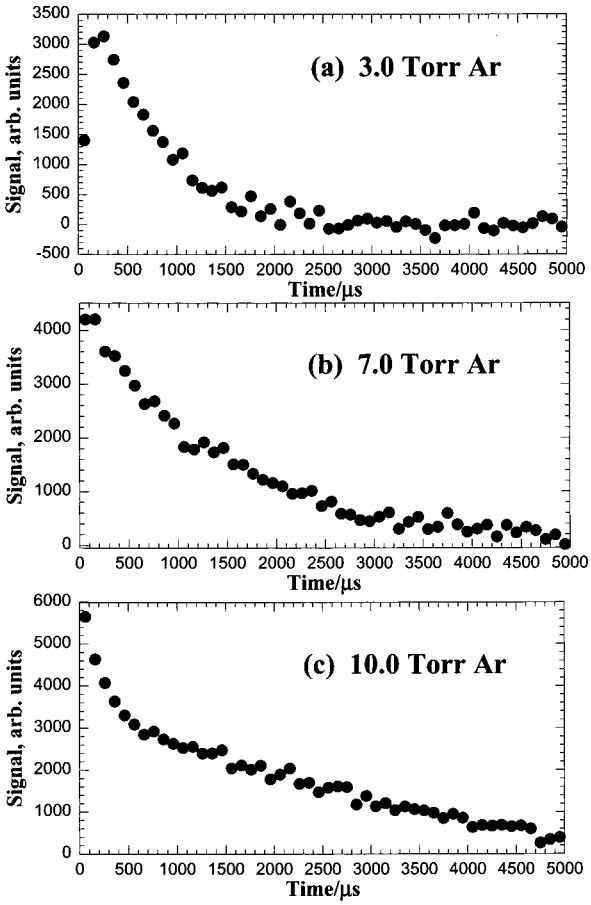


**Figure 2.** $NO_2$ LIF signals (arbitrary units) from the photolysis of PNA. Fluorescence from background $NO_2$, excimer laser-induced cell fluorescence, and probe laser scatter have been subtracted from the temporal profiles. For the three experiments shown, the concentrations of PNA and the Ar buffer gas pressures were (a) $3.4 \times 10^{13}$ molecules $cm^{-3}$ and 3.0 Torr, (b) $9.5 \times 10^{13}$ molecules $cm^{-3}$ and 7.0 Torr, and (c) $1.9 \times 10^{14}$ molecules $cm^{-3}$ and 10.0 Torr. The signal rise observed in (a) and (b) is due to collisional energy transfer from high vibrational levels of the $X(^2A_1)$ state of $NO_2$.[16]

where $\Lambda$ is a detector response function, $\phi_i^{NO_2}(\lambda_{photo})$ is the $NO_2$ quantum yield of the precursor, $i$, which has an initial concentration, $[i]$, and an optical cross section, $\sigma_i(\lambda_{photo})$ at the photolysis wavelength, $\lambda_{photo}$. To avoid the difficulty in having to directly determine $\Lambda$, $HNO_3$ is used as a calibrant. By measuring the $NO_2$ LIF signals from back-to-back experiments with PNA and $HNO_3$ precursors, the detector response function is eliminated, i.e.

$$\frac{[NO_2]_{PNA}}{[NO_2]_{HNO_3}} = \frac{S_{(PNA)}(\tau)}{S_{(HNO_3)}(\tau)} = \frac{\phi_{PNA}^{NO_2}(\lambda_{photo})}{\phi_{HNO_3}^{NO_2}(\lambda_{photo})} \frac{[PNA]}{[HNO_3]} \frac{\sigma_{PNA}(\lambda_{photo})}{\sigma_{HNO_3}(\lambda_{photo})} \quad (3)$$

$S_i(\tau)$ is the fluorescence signal from each of the precursors at time, $\tau$, after photolysis. Since $HNO_3$ photodissociates at 248 nm to produce $NO_2$ product with a quantum yield of unity,[17] eq 3 can be rewritten as

$$\phi_{PNA}^{NO_2}(\lambda_{photo}) = \phi_{HNO_3}^{NO_2}(\lambda_{photo}) \frac{S_{(PNA)}(\tau)}{S_{(HNO_3)}(\tau)} \frac{[HNO_3]}{[PNA]} \frac{\sigma_{HNO_3}(\lambda_{photo})}{\sigma_{PNA}(\lambda_{photo})} \quad (4)$$

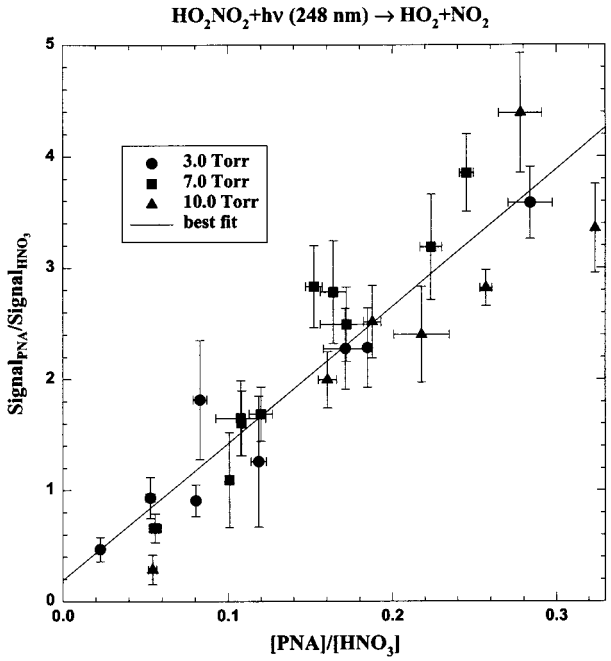


**Figure 3.** Plot of the ratios of $NO_2$ fluorescence from back-to-back 248 nm photolysis experiments using $HNO_3$ and $HO_2NO_2$ as a function of the corresponding relative concentrations of each precursor. The circles, squares, and triangles indicate data obtained at 3.0, 7.0, and 10.0 Torr total pressure, respectively. The $r^2$ value for the least-squares fit is 0.85.

The recommended cross sections,[5] $\sigma_{HNO_3}(248\ nm) = 2.00 \times 10^{-20}$ $cm^2$ $molecule^{-1}$ and $\sigma_{PNA}(248\ nm) = 4.58 \times 10^{-19}$ $cm^2$ $molecule^{-1}$, were used to obtain $\phi_{PNA}^{NO_2}$. To determine the relative production of $NO_2$ from each precursor, the time-dependent fluorescence signals from both $HNO_3$ and PNA were ratioed and averaged at set delays between the photolysis and probe pulses. This ratio of independent values gives the relative yield of $NO_2$, $S_{PNA}(\tau)/S_{HNO_3}(\tau)$, for eq 4. This procedure was repeated for all sets of data. The results of the measurements made at total flows $\geq$700 sccm are plotted versus the ratio of the precursor concentrations in Figure 3. Results for flows $<$700 sccm were not used as discussed in the next section. Each data point represents a temporally averaged ratio of LIF signals. The vertical error bars were determined by the statistical error in the signal ratio, while the horizontal error bars were dominated by the uncertainty in the PNA concentration measurement. The line represents the linear regression of these data points and has a slope $= S_{PNA}(\tau)/S_{HNO_3}(\tau) \times [HNO_3]/[PNA] = 12.3 \pm 1.0$. Substituting this value and the PNA and $HNO_3$ concentrations calculated from the UV absorption measurements into eq 4 results in a quantum yield of 0.56 for the production of $NO_2$ from PNA photolysis at 248 nm. The results of all data sets are tabulated in Table 1.

## Discussion

As stated above, the quantum yield of $NO_2$ production from PNA photolysis was determined by solving eq 4 using LIF data collected over a variety of PNA and $HNO_3$ concentrations at total flow rates greater than 700 sccm and at total pressures of 3.0, 7.0, and 10.0 Torr. The data shown in Figure 3 are independent of total pressure and linear over the concentration ranges employed. This is in contrast to LIF data collected at similar pressures and flows of 500 sccm, which exhibited a marked pressure dependence (see Table 1). This dependence is attributed to decomposition of PNA on the walls as results of the longer residence times.

**TABLE 1: Measurement Conditions and Results for 248 nm PNA Photolysis Experiments**

| pressure, Torr | flow rate, sccm | no. of measurements | slope | [PNA], $10^{13}$ molecules $cm^{-3}$ | [$HNO_3$], $10^{14}$ molecules $cm^{-3}$ |
|---|---|---|---|---|---|
| 3.0 | 500 | 13 | 14.4 | 2.6−31 | 4.9−36 |
| | 700−900 | 8 | 11.4 | 1.4−12 | 1.8−23 |
| 7.0 | 500 | 17 | 8.3 | 2.3−41 | 7.7−81 |
| | 700−1400 | 10 | 16.6 | 7.7−29 | 4.2−23 |
| 10.0 | 500 | 5 | 5.3 | 4.6−14 | 6.9−21 |
| | 700−900 | 7 | 9.2 | 14−43 | 5.9−17 |

Evidence of diffusion, fluorescence quenching, and collisional deactivation of the internally excited nascent $NO_2$ photoproduct is seen in the LIF profiles (Figure 2) at short time scales. Similar profiles were obtained in the earlier studies with $HNO_3$ and PAN.[16−18] At total pressures of 3.0 Torr, the vibrational relaxation of $NO_2$ was not completed before the first LIF data was recorded and hence there is an observable initial growth in the LIF signal. This growth is much less pronounced in the 7.0 Torr data and is not detectable by 10.0 Torr. Fluorescence quenching is more efficient at 10.0 Torr total pressure, however, so the maximum signal for comparable PNA or $HNO_3$ concentrations is less than that at lower pressures. For measurements conducted at constant flow rates, but varying total pressures (such as those in Figure 2), the effects of diffusion out of the viewing zone can be detected. The fluorescence decay at 3.0 Torr is more rapid than at 10.0 Torr due to the faster diffusion and decreased residence time in the photolysis cell.

Finally, we report a quantum yield for the production of $NO_2$ from PNA photolysis of $0.56 \pm 0.17$ ($2\sigma$). The stated uncertainty includes the uncertainty in the slope of Figure 3 (16%), the uncertainty in the *relative* cross sections for $HNO_3$ and PNA at the photolysis and analysis wavelengths (10%), and the uncertainties in the on-line UV absorbance measurements for $HNO_3$ and PNA (10% and 20%, respectively). The derived quantum yield is somewhat lower than the value inferred from the results of MacLeod et al.,[11] but is within the stated errors and can be considered to be in agreement considering the complexity of the reaction mechanism invoked to interpret the measurements of MacLeod et al.[11] The most difficult part of the earlier study was associated with characterizing the purity and amounts of PNA using mass spectrometric techniques. This problem was circumvented, in part, in this study by measuring the vapor concentrations in situ via UV absorption and by incorporating the results from off-line FTIR and the near-IR experiment. Another consideration in this regard is that the current work and the MacLeod et al. study may be influenced by dissociation of hot photofragments. In this study, $NO_2$ can be formed from the decomposition of excited $NO_3$ (channel 1e) and removed by decomposition of excited $NO_2$ (channel 1f). The measurement of OH in the MacLeod et al. work may be influenced by the decomposition of excited $HO_2$ (channel 1e). These effects may be responsible for the failure of the observed OH and $NO_2$ quantum yields to sum to unity at 248 nm. Both experiments, however, measure the quantities that are important for the purposes of atmospheric modeling.

**Calculations of Potential Energy Surfaces.** The optimized geometry of the $HO_2NO_2$ ground state is shown in Figure 4. The optimized results of calculations at the CCSD(T)/cc-pVDZ level of theory indicate that the ground state of $HO_2NO_2$ has no symmetry and that all the heavy atoms lie approximately in one plane. The electronic configurations for the singlet and triplet states in this study are summarized in Table 2. The configuration of the ground state is

$$(\text{core})^{10}(1-17)a^2 18a^2 19a^2 20a^2 21a^0 22a^0 23a^0$$

The core consists of molecular orbitals formed by the 1s orbitals of the five heavy atoms. 18a is a nonbonding molecular orbital with contributions from the 2p orbitals of the two oxygen atoms of $NO_2$ and lies approximately perpendicular to the molecular plane. The 19a and 20a molecular orbitals are the nonbonding molecular orbitals consisting mainly of the 2p orbitals of the two oxygen atoms in the $NO_2$ group. These orbitals lie in the heavy atom plane. The 21a orbital is the $\pi$-type antibonding MO formed from the 2p orbitals of the two oxygen atoms and the nitrogen atom of the $NO_2$ group, and is perpendicular to the heavy atom plane. The excited states, $2^1A$, $3^1A$, $1^3A$, and $2^3A$, are derived from the single electronic transitions 20a → 21a, 19a → 21a, 18a → 21a, and 20a → 21a, separately. The excited states studied in this work can be described as n → $\pi^*$ transitions on the $NO_2$ group.

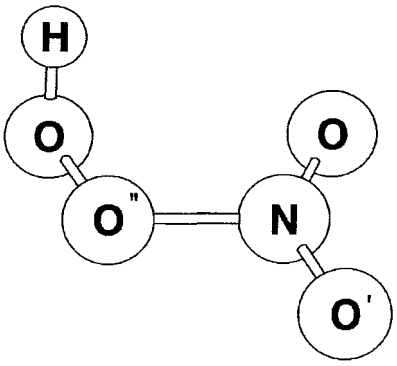


**Figure 4.** Optimized structure of $HO_2NO_2$. Detailed geometrical parameters are given in Table 4.

**TABLE 2: Electronic Configurations of $HO_2NO_2$ Singlet and Triplet States**

| state | electronic configuration |
|---|---|
| $1^1A$ | $(\text{core})^{10}(1-17)a^2 18a^2 19a^2 20a^2 21a^0 22a^0 23a^0$ |
| $2^1A$ | 20a → 21a |
| $3^1A$ | 19a → 21a |
| $1^3A$ | 18a → 21a |
| $2^3A$ | 20a → 21a |

**TABLE 3: Vertical Excitation Energies (VEEs), in eV**

| | CASSCF | MRCI |
|---|---|---|
| state | VEE(cc-pVDZ) | VEE(cc-pVDZ) |
| $1^1A$ | 0.0 | 0.0 |
| $2^1A$ | 4.78 | 5.05 |
| $3^1A$ | 5.41 | 5.52 |
| $1^3A$ | 4.03 | 4.26 |
| $2^3A$ | 4.57 | 4.76 |

As shown in Table 3, the vertical excitation energy for the $2^1A$ state is 5.05 eV (246 nm). This is somewhat smaller than the value of 5.823 eV (5.610 eV with electron correlation) obtained by Saxon and Liu using the CI singlet method with the DZP basis set.[30] Recently, Chen and Hamilton calculated the vertical excitation energies of the lowest singlet state to be 5.041 and 4.903 eV with CAS and CASPT2 wave functions, respectively, using the B3LYP/6-31G* geometry.[31] Our results are consistent with both the CAS and CASPT2 results of Chen and Hamilton. The present results are also consistent with the

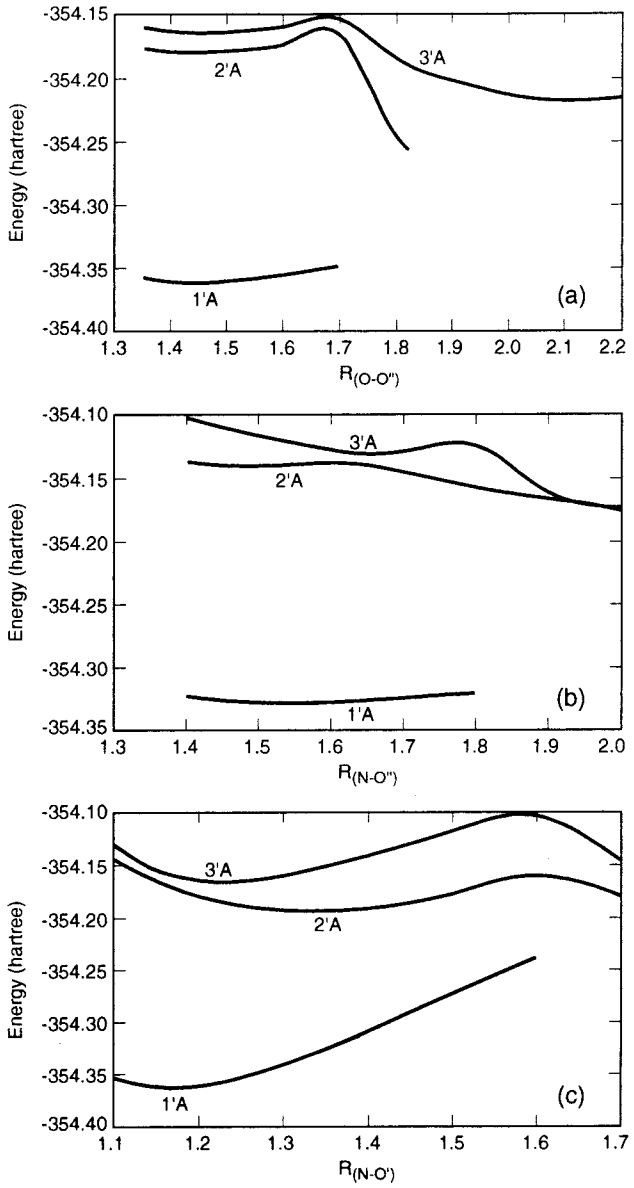


**Figure 5.** Potential energy curves of $HO_2NO_2$ in the Franck−Condon region along the O−O″ (a), N−O″ (b), and N−O′ (c) coordinates. Energies are in hartrees and coordinate distances are in angstroms.

presence of a small feature in the absorption spectrum at 250 ± 10 nm (4.97 eV).[9]

The potential energy curves calculated for the three singlet states along the $R_{O-O''}$, $R_{N-O''}$, and $R_{N-O'}$ coordinates are shown in Figure 5a−c. As can be seen in Figure 5a, the lowest singlet excited states, $2^1A$ and $3^1A$, are weakly bound along the $R_{O-O''}$ coordinate in the Franck−Condon region (defined as the region within 0.25 Å of the equilibrium point in the ground state). Their potential energy curves indicate, however, that there are crossings which could lead to predissociation arising from intersections with other unbound states. Along the $R_{N-O''}$ coordinate, the potential energy curve for the $2^1A$ state is shallower than the curve for the $R_{O-O''}$ coordinate in the Franck−Condon region and intersects with other unbound states leading to predissociation. The $3^1A$ state is bound and also intersects with other unbound states around the Franck−Condon region. Referring to the $2^1A$ and $3^1A$ potentials, the states are more strongly bound in the Franck−Condon region along the $R_{N-O'}$ coordinate than along the $R_{O-O''}$ and $R_{N-O''}$ coordinates. The slopes of the potential curves also vary more rapidly with $R_{N-O'}$ than with $R_{O-O''}$ and $R_{N-O''}$. This is because the relevant electronic transition, n → π*, is located primarily on the $NO_2$ moiety. Also, the crossings between the $2^1A$ and $3^1A$ states and the repulsive states occur at larger values of internuclear separation on the N−O′ coordinate than on the O−O″ and N−O″ coordinates. As noted above, inclusion of diffuse functions in the basis set did not significantly affect the potentials along the O−O″ coordinate.

**TABLE 4: Optimized Geometries for the Ground and Lowest Triplet State of $HO_2NO_2$ (Bond Lengths in Å, Angles in deg, Energy in Hartrees)**

| | CCSD(T)/cc-pVDZ | |
|---|---|---|
| parameters | ground state | lowest triplet state |
| NO | 1.200 | 1.292 |
| NO′ | 1.200 | 1.294 |
| NO″ | 1.518 | 1.515 |
| OO″ | 1.418 | 1.427 |
| OH | 0.975 | 0.976 |
| ∠ONO | 133.6 | 108.7 |
| ∠O″NO | 109.9 | 108.9 |
| ∠OON | 108.1 | 104.4 |
| ∠HOO | 101.6 | 100.7 |
| ∠OO″NO | −12.2 | −53.7 |
| ∠HOON | 84.2 | 82.2 |
| energy | −355.19609 | −355.08444 |

The calculated potential energy curves in Figure 5 provide a way to rationalize the observed PNA photolysis quantum yields. At 248 nm, $HO_2NO_2$ dissociation through the $NO_2$ moiety is unfavorable because there is no curve crossing in the Franck−Condon region along the $R_{N-O'}$ coordinate for the $2^1A$ excited state. There is curve crossing in the Franck−Condon region for the weakly bound $2^1A$ state along the $R_{O-O''}$ coordinate, and any leakage could predissociate along the $R_{O-O''}$ coordinate to produce OH + $NO_3$. There is curve crossing in the Franck−Condon region for the $2^1A$ state along the $R_{N-O''}$ coordinate which leads to the formation of $HO_2$ + $NO_2$ by predissociation. Comparing Figure 5a and Figure 5b, we can see that photodissociation yields along the $R_{N-O''}$ coordinate should be greater than along the $R_{O-O''}$ coordinate because the N−O″ surface is shallower and curve crossing occurs at smaller internuclear separations. This is consistent with the observed quantum yields of 0.34 for OH formation[11] and 0.56 for $NO_2$ formation at 248 nm.

The vertical excited state energies of the triplet states are summarized in Table 3. The two lowest triplet states lie below the lowest excited singlet state. The energy of the lowest triplet state is estimated to be 4.26 eV. The next triplet state lies about 0.5 eV above the $1^3A$ state. The triplet excited states all have predominantly valence character. Both the triplet states of $HO_2$-$NO_2$ involve promotion into an orbital with antibonding character in the $NO_2$ chromophore, as is the case for the corresponding second and third singlet excited states. To obtain a better understanding of the band origin of the lowest triplet state, the geometry of this state was optimized at the CCSD-(T)/cc-pVDZ level of theory. The results for the optimized ground state and lowest triplet state are presented in Table 4. These results show that there is significant internal rotation that occurs around the NO bond (HOO″−$NO_2$). There is also a significant lengthening of the NO bonds on the $NO_2$ group. These changes are consistent with the reduction in bond order associated with the n → π* transition for this state. A recent ab initio study of $HO_2NO_2$ calculated at the MP2(Fc)/6-311++G** level by Jitariu and Hirst [32] shows similar trends in structural changes in the $NO_2$ group upon excitation into the triplet state. The adiabatic singlet−triplet ($S_0$−$T_1$) splitting calculated in this

study is 3.04 eV at the CCSD(T)/cc-pVDZ level of theory with zero-point vibrational energy differences included. This is identical to the value of 3.04 eV calculated by Jitariu and Hirst using the G2MP2 method.[32] These results imply that the origin of the singlet−triplet absorption starts around 407 nm.

**Acknowledgment.** We acknowledge the technical support of Mr. Dave Natzic. The supercomputer used in this investigation was provided by funding from the NASA Offices of Earth Science, Aeronautics and Space Science. The research was carried out by the Jet Propulsion Laboratory, California Institute of Technology, under contract with the National Aeronautics and Space Administration. Support from the NASA Upper Atmosphere Research, Tropospheric Chemistry and Atmospheric Effects of Aircraft Programs is acknowledged.

## References and Notes

(1) Johnston, H. S.; Kinnison, D. E.; Wuebbles, D. J. *J. Geophys. Res.* **1989**, *94*, 16351−16364.
(2) *Aviation and the Global Atmosphere*; Penner, J. E., Lister, D. H., Eds.; Cambridge University Press: Cambridge, 1999.
(3) WMO *Scientific Assessment of Ozone Depletion: 1998*; World Meteorological Organization: Geneva, 1999.
(4) IPCC *Climate Change 1995*; Cambridge University Press: Cambridge, 1996.
(5) DeMore, W. B.; Sander, S. P.; Golden, D. M.; Hampson, R. F.; Kurylo, M. J.; Howard, C. J.; Ravishankara, A. R.; Kolb, C. E.; Molina, M. J. *Chemical Kinetics and Photochemical Data for Use in Stratospheric Modeling, Evaluation Number 12*; Jet Propulsion Laboratory: California Institute of Technology, 1997.
(6) Cox, R. A.; Patrick, R. *Int. J. Chem. Kinet.* **1979**, *11*, 635.
(7) Morel, O.; Simonaitis, R.; Heicklen, J. *Chem. Phys. Lett.* **1980**, *73*, 38.
(8) Graham, R. A.; Winer, A. M.; Pitts, J. N., Jr. *Geophys. Res. Lett.* **1978**, *5*, 909.
(9) Molina, L. T.; Molina, M. J. *J. Photochem.* **1981**, *15*, 97.
(10) Singer, R. J.; Crowley, J. N.; Burrows, J. P.; Schneider, W.; Moortgat, G. K. *J. Photochem. Photobiol.* **1989**, *48*, 17−32.
(11) MacLeod, H.; Smith, G. P.; Golden, D. M. *J. Geophys. Res.* **1988**, *93*, 3813−3823.
(12) Donaldson, D. J.; Frost, G. J.; Rosenlof, K. H.; Tuck, A. F.; Vaida, V. *Geophys. Res. Lett.* **1997**, *24*, 2651−2654.
(13) Wennberg, P. O.; Salawitch, R. J.; Donaldson, D. J.; Hanisco, T. F.; Lanzendorf, E. J.; Perkins, K. K.; Lloyd, S. A.; Vaida, V.; Gao, R. S.; Hintsa, E. J.; Cohen, R. C.; Swartz, W. H.; Kusterer, T. L.; Anderson, D. E. *Geophys. Res. Lett.* **1999**, *26*, 1373−1376.
(14) Fono, L.; Donaldson, D. J.; Proos, R. J.; Henry, B. R. *Chem. Phys. Lett.* **1999**, *311*, 131−138.
(15) Zhang, H.; Roehl, C. M.; Sander, S. P.; Wennberg, P. O. *J. Geophys. Res.* **2000**, *105*, 14593−14598.
(16) Mazely, T. L.; Friedl, R. R.; Sander, S. P. *J. Chem. Phys.* **1994**, *100*, 8040−8046.
(17) Mazely, T. L.; Friedl, R. R.; Sander, S. P. *J. Phys. Chem.* **1995**, *99*, 8162−8169.
(18) Mazely, T. L.; Friedl, R. R.; Sander, S. P. *J. Phys. Chem.* **1997**, *101*, 7090−7097.
(19) Kenley, R. A.; Trevor, P. L.; Lan, B. Y. *J. Am. Chem. Soc.* **1981**, *103*, 2203.
(20) May, R. D.; Friedl, R. R. *J. Quant. Spectrosc. Radiat. Transfer* **1993**, *50*, 257−266.
(21) Hojer, S.; May, R. D.; Miller, C. E. *J. Quant. Spectrosc. Radiat. Transfer* **1996**, *55*, 273−278.
(22) Li, Z.; Friedl, R. R.; Moore, S. B.; Sander, S. P. *J. Geophys. Res.* **1996**, *101*, 6795−6802.
(23) *Handbook of Chemistry and Physics*, 71st ed.; Lide, D. R., Ed.; CRC Press: Boca Raton, FL, 1990.
(24) Watts, J. D.; Gauss, J.; Bartlett, R. J. *J. Chem. Phys.* **1993**, *98*, 8718−8733.
(25) Dunning, T. H. *J. Chem. Phys.* **1989**, *90*, 1007−1023.
(26) Werner, H. J.; Knowles, P. J. *J. Chem. Phys.* **1985**, *82*, 5053−5063.
(27) Knowles, P. J.; Werner, H. J. *Chem. Phys. Lett.* **1985**, *115*, 259−267.
(28) Werner, H. J.; Knowles, P. J. *J. Chem. Phys.* **1988**, *89*, 5803−5814.
(29) Knowles, P. J.; Werner, H. J. *Chem. Phys. Lett.* **1988**, *145*, 514−522.
(30) Saxon, R. P.; Liu, B. *J. Phys. Chem.* **1985**, *89*, 1227−1232.
(31) Chen, Z.; Hamilton, T. P. *J. Phys. Chem.* **1996**, *100*, 15731−15734.
(32) Jitariu, L. C.; Hirst, D. M. *J. Phys. Chem. A* **1999**, *103*, 6673−6677.